EXPERIMENTAL INVESTIGATION OF HYDRAULIC RAM

Larry Scott Mueller

NAVAL POSTGRADUATE SCHOOL
Monterey, California

THESIS

EXPERIMENTAL INVESTIGATION OF HYDRAULIC RAM

by

Larry Scott Mueller

Thesis Advisor: Allen E. Fuhs

March 1974

Experimental Investigation of Hydraulic Ram

by

Larry Scott Mueller
Captain, U.S. Marine Corps
B.S. AeE, University of Minnesota, 1967

Submitted in partial fulfillment of the
requirements for the degree of

MASTER OF SCIENCE IN AERONAUTICAL ENGINEERING

from the

NAVAL POSTGRADUATE SCHOOL
March 1974

ABSTRACT

Extensions of the investigations aimed at preventing aircraft destruction through the effects of hydraulic ram were conducted. By analyzing spark shadowgraphs the existence of a family of transient shock waves was confirmed. These shock waves were created by a surface anomaly in a projectile and are not unlike those found in fragmentary warheads. In an attempt to measure wall deflections subsequent to projectile impact, a system based on optical fiber proximity probes was investigated. Mathematical models based on grid distortions were used as a means of calculating shock wave pressures. The AFIT thesis correlating cavity size, energy and radius to underwater explosions was verified from an analysis of 16 mm films.

TABLE OF CONTENTS

LIST OF TABLES

LIST OF FIGURES

ACKNOWLEDGEMENTS

The author would like to express his grateful appreciation for the leadership and technical guidance offered by his thesis advisor, Professor Allen E. Fuhs, and to the Aeronautics Department Technician Staff for their assistance in assembling the test apparatus.

I. INTRODUCTION

The term hydraulic ram has been historically associated with the various waves causing, usually, catastrophic failure of an aircraft fuel cell when penetrated by a projectile.

When a projectile or fragment with high velocity impacts the surface of a liquid medium, a disturbance is produced which spreads throughout the medium. The disturbance is characterized by a region of increased pressure and density together with a small forward motion of the fluid. When the energy of the disturbance is large, the disturbance travels as a surface of discontinuity and is called a shock wave. (Ref. 1). Typically the shock wave phenomenon has been identified as the first phase of hydraulic ram.

As projectile penetration continues, a pressure field is created that tends to displace the fluid from the projectile, transforming projectile energy to kinetic energy of the fuel. This is the beginning of the cavity phase.

The phenomenon associated with these two phases has been studied for as long as three wars i.e. 1947 through present. Recent investigations into fragment-induced shock waves and cavities have been initiated, the results of which are leading to a more clear understanding of hydraulic ram.

II. SHOCK PHASE EXPERIMENTS

A. WAVE GENERATION IN SHOCK PHASE BY FRAGMENTARY PROJECTILES

Previous experiments conducted at NPS involving the impacting of 0.22 caliber projectiles into a water-filled tank produced shadowgraphs such as those shown as Figures 1 and 2. Figure 1 is the projectile in free flight, whereas Figure 2 shows the family of waves created after impact. The flow features visible in Figure 2 are considered to be:

1. projectile wake,
2. reflected bandwave,
3. reflected bow wave,
4. incident wake recompression shock,
5. incident bandwave,
6. transient entry shock,
7. secondary transient shock wave (see discussion below).

In Figure 2, items 6 to 9 occur in the water internal to the tank and items 1 to 5 occur in the air external to the tank. The dense, thick region in each shadowgraph is the test tank wall. Region 8 is the projectile's cavity and item 9 is the grid distortion used to determine the medium's density. The spark shadowgraph method was used as it has the advantage of showing the projectile-induced waves at one observation. Of particular interest was the formation of the wave 7, in Figure 2, which was investigated as follows.

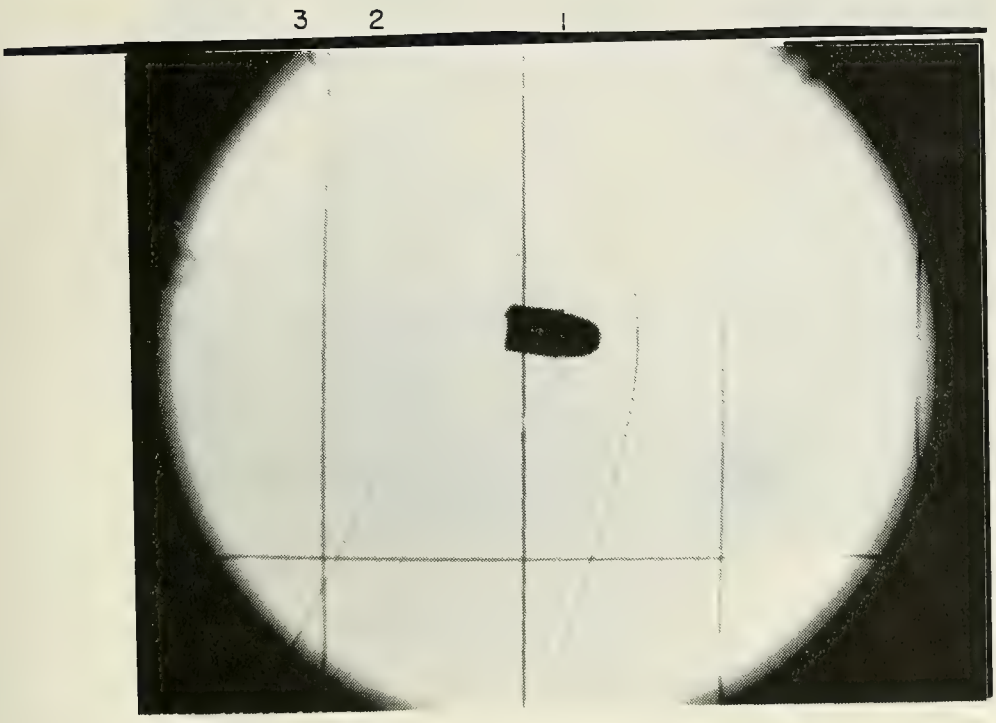

Fig. 1 0.22 Caliber Projectile in Free Flight

1. Bow Shock Wave

2. Band Shock Wave

3. Wake Recompression Shock

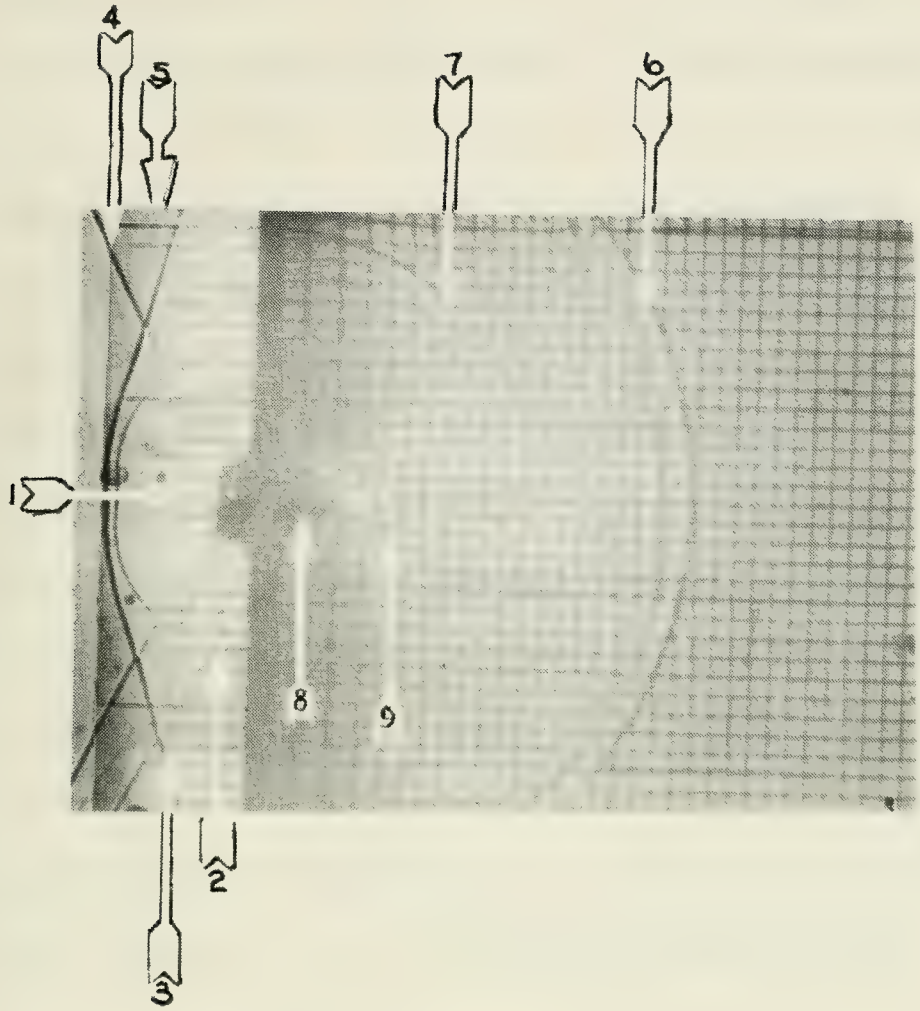

Fig. 2 Waves Generated From Projectile Impact

A randomly selected, factory loaded 0.22 cal projectile has the geometry shown in Figure 3. The volume of the projectile's nose was calculated using successive truncated cones while the portion aft of the shoulder was calculated assuming a solid cylinder. Assuming a constant velocity immediately after penetration into the tank, the rate of volume penetration was plotted against distance along the projectile's centerline, Figure 4. The discontinuity in Figure 4 appears at a longitudinal distance of 0.20 inches and corresponds to the distance where the projectile itself has a discontinuity, i.e., the shoulder. This shoulder is the origin of bandwave shown in Figure 1. This suggests that although the surface irregularity is small (0.020 inches), it is still capable of creating secondary transient shock waves. It is concluded that the wave 7 in question on Figure 2 is indeed a secondary transient entry shock. Reference 2 describes the deformation of several previous test rounds. Considering their fragmentary shape it could be expected that fuel cells punctured by fragmentation warheads would be subjected to a myriad of such secondary shocks.

B. PRESSURE BY GRID DISTORTION

Figure 5 is a shadowgraph of a fine-mesh grid taken while the fluid was at rest. No grid distortions are apparent. The projectile's path is from the left to right through the center of the shadowgraph. After penetration the grid in this area is distorted. This region was used in the subsequent analysis.

As the projectile penetrates the water it displaces fluid by compressing it to very high pressures. This disturbance is the transient shock 6 in

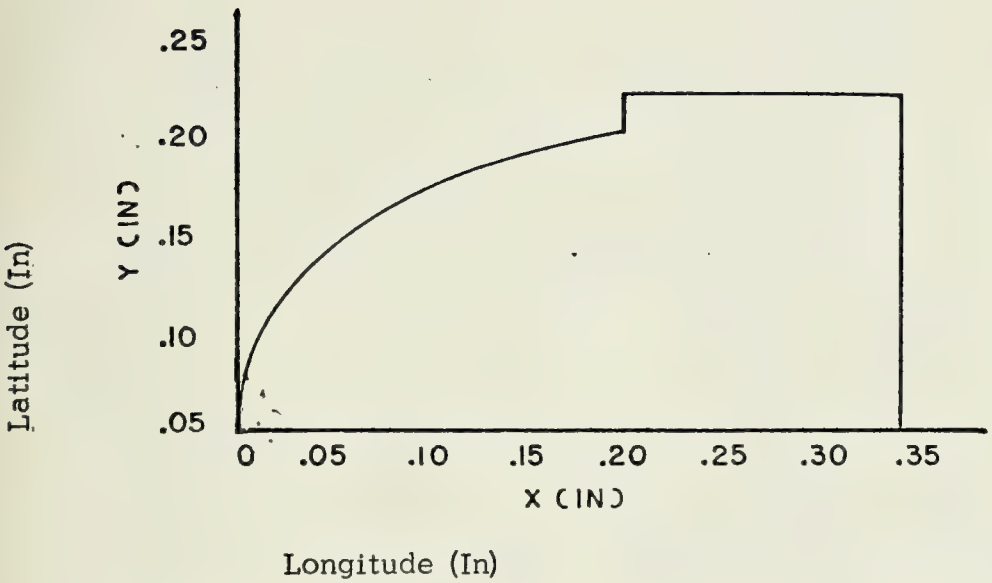

Fig. 3 Geometry of 0.22 Caliber Projectile

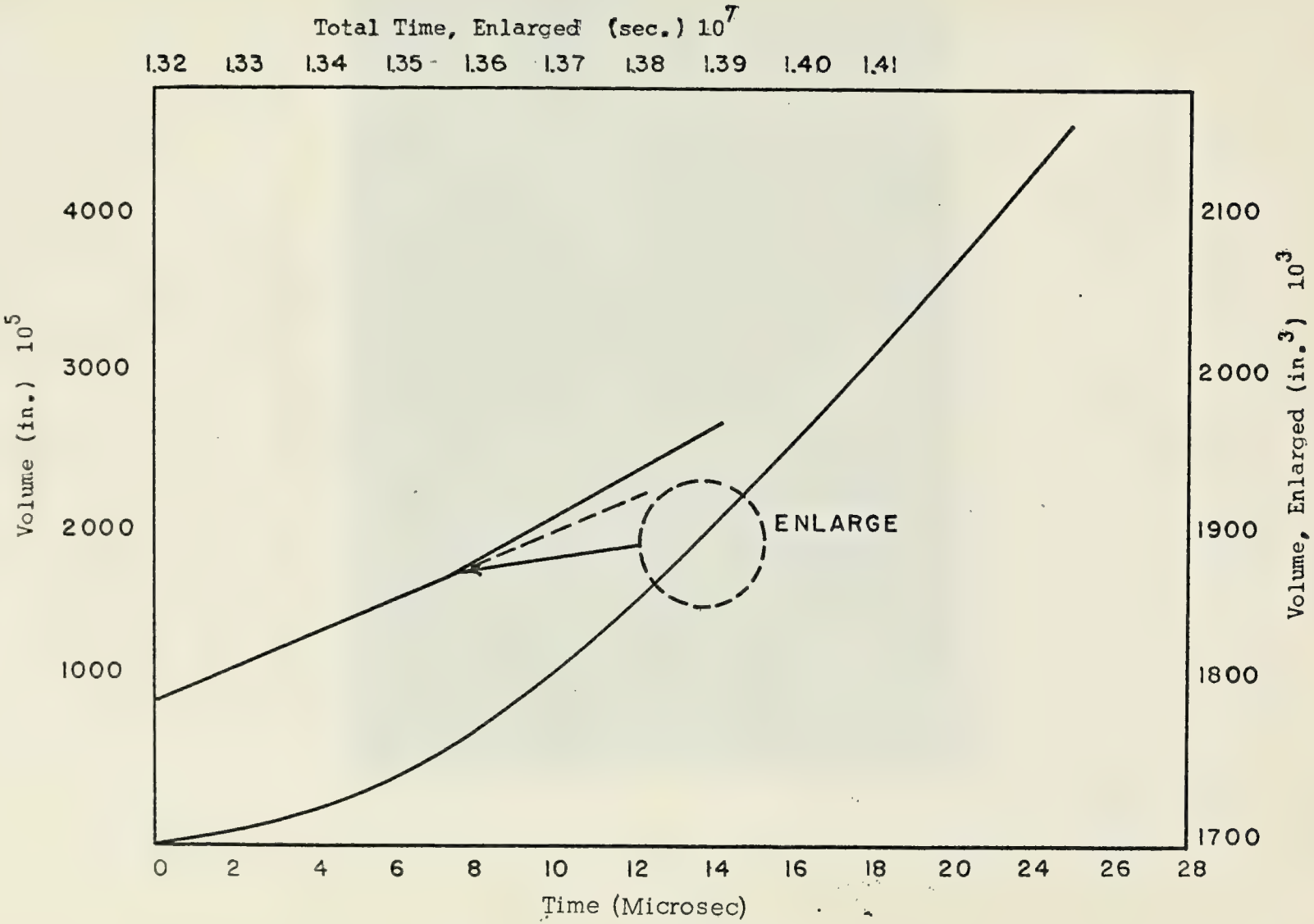

Fig. 4 Volume Penetration vs Time for Projectile

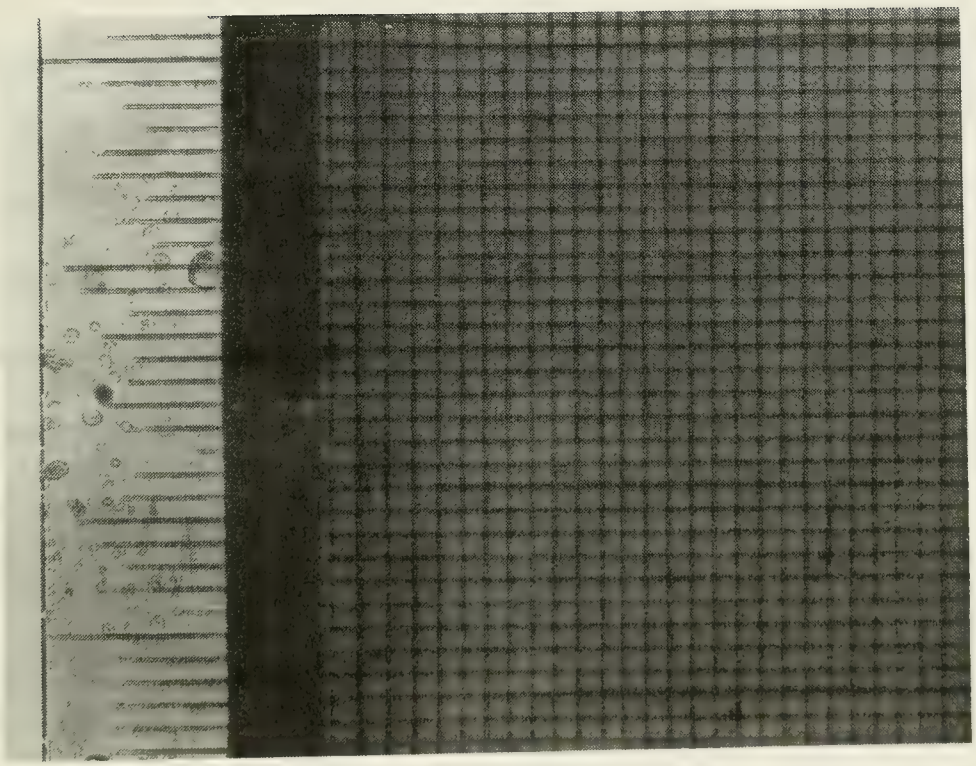

Fig. 5 Fine Mesh Grid Showing Planar Regions

Figure 2. As penetration continues, the transient shock continues to receive energy until the projectile becomes fully wetted; this occurs at 23 microseconds in Figure 4. A rarefaction wave then forms that tends to dissipate the shock wave. (Ref. 3). The localized high shock pressures are known to be of short duration, usually tens of microseconds, and are completely dissipated by the time significant projectile penetration occurs.

The spark shadow-graph could be set off with any time delay up to approximately 30 microseconds. Each shock wave in the shadowgraph reveals a distinct presence-of-light band and an absence-of-light band. The concentration of light around the projectile's transient entry shock is best explained by considering the pressure and density increase due to the shock wave. Similar optical distortion at the nose of the fragment is due to high density at the nose. See Figure 2. The pressure is known to reach values in excess of 4000 kg/cm^2 (56,890 psi), which is sufficient to produce a change in the medium's refractive index. The width of the dark band varies with the pressure in the wave. The fractional change in refractive index, ϵ, has been studied by Poindexter and Rosen and was determined to vary as $\epsilon = 1.06 \times 10^{-5} p$ where p is pressure in kg/cm^2 (Ref. 1). This conforms to an isothermal change, whereas a change produced by the transient shock is more nearly adiabatic (Ref. 1). A value of $\epsilon = 10^{-5} p$ has been justified by McMillen and was used throughout this analysis (Ref. 1). It was also assumed that in a homogeneous medium such as water, light rays have the form of straight lines.

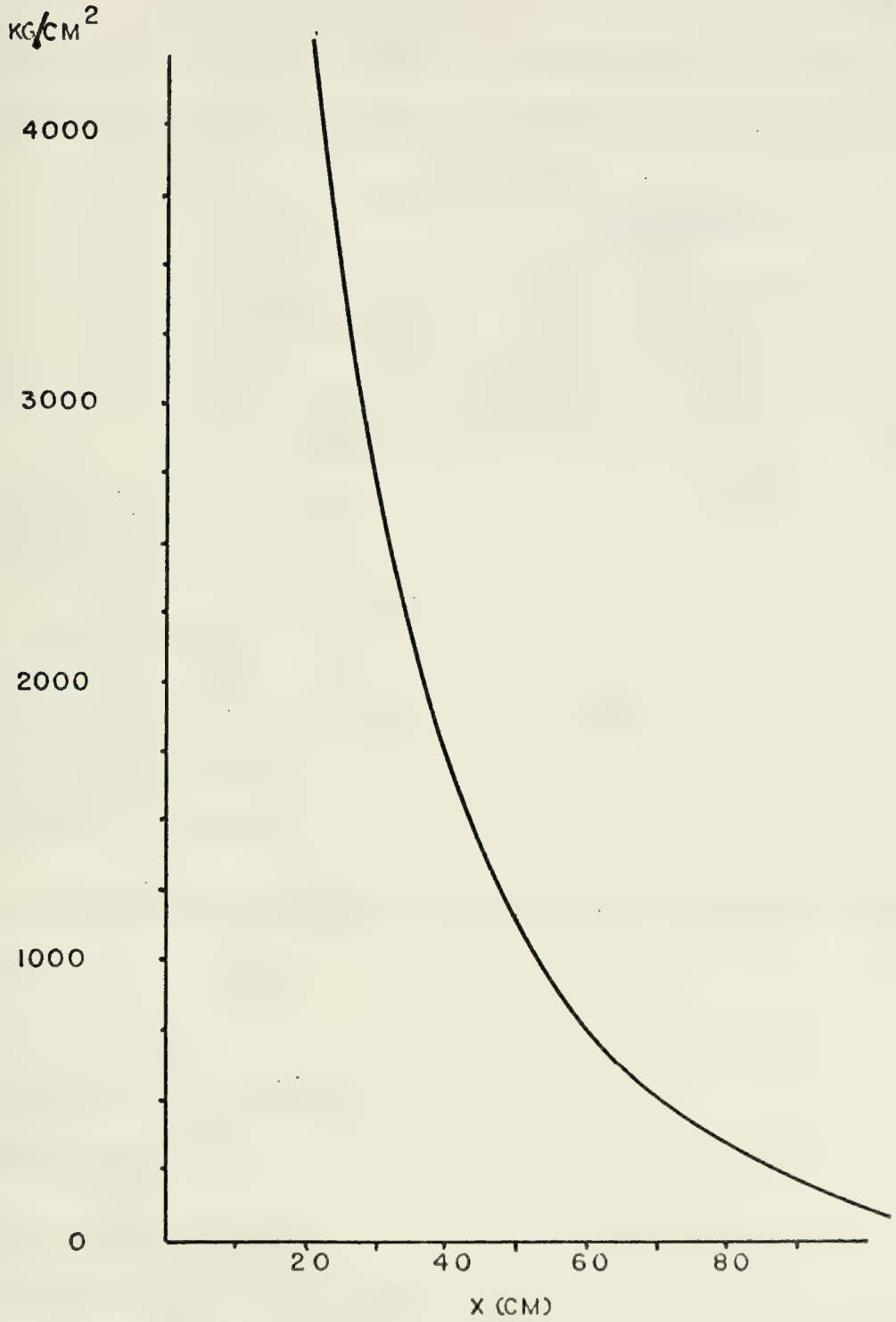

Fig. 6 Shock Front Pressure Generated in Water by Projectile Impact.

Seven shock pressures were extracted from Figure 6. When the projectile had penetrated three cm into the tank the pressure was noted as 2700 kg/cm^2. Define Θ_1 and Θ_2 as the angles which the incident ray and refracted ray make with a normal to the shock wave surface (Fig. 7).

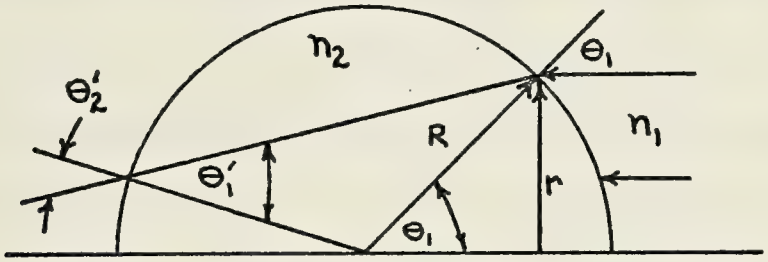

Fig. 7 Light rays in homogeneous regions bounded by a shock wave.

By geometry Θ_1 is given by (1)

$$\sin\Theta_1 = \frac{r}{R}$$

$$\Theta_1 = \sin^{-1}\left(\frac{r}{R}\right)$$

Using Snell's law the angle Θ_2 can be introduced

$$n_2 \sin\Theta_2 = n_1 \sin\Theta_1$$

$$\sin\Theta_2 = \left(\frac{n_1}{n_2}\right)\sin\Theta_1$$

From the previous paragraph the change in refractive index can be expressed as

$$\epsilon = \frac{\Delta n}{n} = \frac{n_2 - n_1}{n_1}$$

$$\therefore n_2 = n_1(1+\epsilon) \quad (2)$$

From equations (1) and (2)

$$\sin\Theta_2 = \left(\frac{1}{1+\epsilon}\right)\left(\frac{r}{R}\right)$$

$$\therefore \Theta_2 = \sin^{-1}\left[\left(\frac{1}{1+\epsilon}\right)\left(\frac{r}{R}\right)\right] \quad (3)$$

and $$2\Delta\Theta = (\Theta_2 - \Theta_1) + (\Theta_2' - \Theta_1') = 2(\Theta_2 - \Theta_1) \quad (4)$$

Note that the changes in angle entering and leaving the shock wave are additive. If the density is homogeneous within the region bounded by the shock wave, as is assumed here, then the high pressure region behaves as a spherical lens. For $\frac{r}{R} = 0.90$ from equation (1), θ_1 is found to be 5.740^{o}. For a pressure of 2700 kg/cm^2, θ_2 is calculated to be 5.588^{o} by equation (3); consequently $2\Delta\theta = 0.303^{o}$. Even for high pressures the angular deflections are small. Calculated values for the remaining six pressures are presented in Table 1. These tabulated results appear reasonable.

The grid distortion analysis assumes rays have spherical symmetry i.e. the refractive index depends only on the distance r from a fixed point 0; see Figure 8.

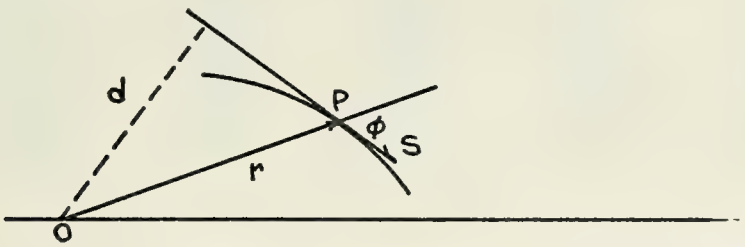

Fig. 8 Illustrating Bouguer's formula nd=constant

For rays situated in a plane through the origin, $nr\sin\phi = c$, where c is a constant. With $d = r\sin\phi$, $nd = c$

This is known as the formula of Bouguer. From geometry, if (r, θ) are the polar coordinates of a plane curve, the angle ϕ between the radius vector to a point P on the same curve and a tangent at P is given by

$$\sin\phi = \frac{r(\theta)}{\sqrt{r^2(\theta) + \left(\frac{dr}{d\theta}\right)^2}}$$

Pressure kg/cm^2	Index of Refraction				
2700.00	1.3659				
RR	THETA1	THETA2	ANS1	ANS2	RES
0.100	0.100	0.098	5.740	5.588	0.303
0.200	0.201	0.196	11.538	11.230	0.615
0.300	0.305	0.296	17.459	16.986	0.946
0.400	0.412	0.400	23.580	22.924	1.312
0.500	0.524	0.508	30.002	29.136	1.732
0.600	0.644	0.624	36.873	35.751	2.243
0.700	0.775	0.750	44.430	42.972	2.917
0.800	0.927	0.893	53.134	51.170	3.928
0.900	1.120	1.068	64.163	61.208	5.909
1112.50	1.3448				
RR	THETA1	THETA2	ANS1	ANS2	RES
0.100	0.100	0.099	5.740	5.676	0.127
0.200	0.201	0.199	11.538	11.409	0.257
0.300	0.305	0.301	17.459	17.261	0.396
0.400	0.412	0.407	23.580	23.305	0.550
0.500	0.524	0.517	30.002	29.639	0.727
0.600	0.644	0.635	36.873	36.401	0.943
0.700	0.775	0.765	44.430	43.816	1.229
0.800	0.927	0.913	53.134	52.301	1.665
0.900	1.120	1.098	64.163	62.890	2.545
750.00	1.3400				
RR	THETA1	THETA2	ANS1	ANS2	RES
0.100	0.100	0.099	5.740	5.697	0.086
0.200	0.201	0.200	11.538	11.451	0.174
0.300	0.305	0.302	17.459	17.325	0.268
0.400	0.412	0.408	23.580	23.394	0.372
0.500	0.524	0.519	30.002	29.756	0.492
0.600	0.644	0.638	36.873	36.553	0.638
0.700	0.775	0.768	44.430	44.014	0.833
0.800	0.927	0.917	53.134	52.569	1.130
0.900	1.120	1.105	64.163	63.296	1.734

Table 1 Angular deflection of light ray by a spherical shock wave for various shock wave pressures

RR	Nondimensional radius
Thetal	Entry angle, radians
Theta2	Exit angle, radians
Ansl	Entry angle, degrees
Ans2	Exit angle, degrees
Res	2(ANSl-ANS2)

Pressure kg/cm2	Index of Refraction				
500.00	1.3366				
RR	THETA1	THETA2	ANS1	ANS2	RES
0.100	0.100	0.100	5.740	5.711	0.057
0.200	0.201	0.200	11.538	11.480	0.116
0.300	0.305	0.303	17.459	17.369	0.179
0.400	0.412	0.409	23.580	23.456	0.249
0.500	0.524	0.521	30.002	29.838	0.329
0.600	0.644	0.640	36.873	36.659	0.427
0.700	0.775	0.771	44.430	44.152	0.557
0.800	0.927	0.921	53.134	52.756	0.757
0.900	1.120	1.110	64.163	63.580	1.165
325.00	1.3343				
RR	THETA1	THETA2	ANS1	ANS2	RES
0.100	0.100	0.100	5.740	5.721	0.037
0.200	0.201	0.201	11.538	11.500	0.076
0.300	0.305	0.304	17.459	17.401	0.117
0.400	0.412	0.410	23.580	23.499	0.162
0.500	0.524	0.522	30.002	29.895	0.214
0.600	0.644	0.641	36.873	36.734	0.278
0.700	0.775	0.772	44.430	44.249	0.363
0.800	0.927	0.923	53.134	52.887	0.493
0.900	1.120	1.113	64.163	63.782	0.761
212.50	1.3328				
RR	THETA1	THETA2	ANS1	ANS2	RES
0.100	0.100	0.100	5.740	5.727	0.024
0.200	0.201	0.201	11.538	11.513	0.050
0.300	0.305	0.304	17.459	17.421	0.076
0.400	0.412	0.411	23.580	23.527	0.106
0.500	0.524	0.522	30.002	29.932	0.140
0.600	0.644	0.642	36.873	36.782	0.182
0.700	0.775	0.773	44.430	44.311	0.238
0.800	0.927	0.924	53.134	52.972	0.323
0.900	1.120	1.115	64.163	63.913	0.499

Table 1 Angular deflection of light ray by a spherical shock wave for various shock wave pressures

RR Nondimensional radius
Thetal Entry angle, radians
Theta2 Exit angle, radians
Ansl Entry angle, degrees
Ans2 Exit angle, degrees
Res 2(ANSl-ANS2)

Pressure kg/cm^2	Index of Refraction				
0.0	1.3300				
RR	THETA1	THETA2	ANS1	ANS2	RES
0.100	0.100	0.100	5.740	5.740	0.0
0.200	0.201	0.201	11.538	11.538	0.0
0.300	0.305	0.305	17.459	17.459	0.0
0.400	0.412	0.412	23.580	23.580	0.0
0.500	0.524	0.524	30.002	30.002	0.0
0.600	0.644	0.644	36.873	36.873	0.0
0.700	0.775	0.775	44.430	44.430	0.0
0.800	0.927	0.927	53.134	53.134	0.0
0.900	1.120	1.120	64.163	64.163	0.0
0.0	1.3300				
RR	THETA1	THETA2	ANS1	ANS2	RES
0.100	0.100	0.100	5.740	5.740	0.0
0.200	0.201	0.201	11.538	11.538	0.0
0.300	0.305	0.305	17.459	17.459	0.0
0.400	0.412	0.412	23.580	23.580	0.0
0.500	0.524	0.524	30.002	30.002	0.0
0.600	0.644	0.644	36.873	36.873	0.0
0.700	0.775	0.775	44.430	44.430	0.0
0.800	0.927	0.927	53.134	53.134	0.0
0.900	1.120	1.120	64.163	64.163	0.0
0.0	1.3300				
RR	THETA1	THETA2	ANS1	ANS2	RES
0.100	0.100	0.100	5.740	5.740	0.0
0.200	0.201	0.201	11.538	11.538	0.0
0.300	0.305	0.305	17.459	17.459	0.0
0.400	0.412	0.412	23.580	23.580	0.0
0.500	0.524	0.524	30.002	30.002	0.0
0.600	0.644	0.644	36.873	36.873	0.0
0.700	0.775	0.775	44.430	44.430	0.0
0.800	0.927	0.927	53.134	53.134	0.0
0.900	1.120	1.120	64.163	64.163	0.0

Table 1 Angular deflection of light ray by a spherical shock wave for various shock wave pressures

RR Nondimensional radius
Thetal Entry angle, radians
Theta2 Exit angle, radians
Ansl Entry angle, degrees
Ans2 Exit angle, degrees
Res 2(ANSl-ANS2)

It is possible to eliminate ϕ by introducing the constant c, as can be seen by the following manipulations:

$$\frac{c}{nr} = \frac{r}{\left[r^2 + \left(\frac{dr}{d\theta}\right)^2\right]^{\frac{1}{2}}}$$

$$\therefore c = \frac{nr^2}{\left[r^2 + \left(\frac{dr}{d\theta}\right)^2\right]^{\frac{1}{2}}}$$

$$c^2 = \frac{n^2 r^4}{r^2 + \left(\frac{dr}{d\theta}\right)^2}$$

$$\therefore r^2 + \left(\frac{dr}{d\theta}\right)^2 = \frac{n^2 r^4}{c^2}$$

$$\text{or } \left(\frac{dr}{d\theta}\right)^2 = \frac{r^2}{c^2}\left[n^2 r^2 - c^2\right]$$

$$\therefore \frac{dr}{d\theta} = \frac{r}{c}\left[n^2 r^2 - c^2\right]^{\frac{1}{2}}$$

$$d\theta = \frac{dr}{\frac{r}{c}\left[n^2 r^2 - c^2\right]^{\frac{1}{2}}}$$

$$\theta = c\int \frac{dr}{r\left[n^2 r^2 - c^2\right]^{\frac{1}{2}}}$$

$$\therefore \theta(r) = \theta' + \frac{c}{\sqrt{A^2 - c^2}} \ln \frac{r'}{r}$$

The assumption of constant pressure behind the shock wave is not realistic. At this point, the assumption of uniform conditions behind the shock wave can be abandoned by introduction of equation (5). In equation (5), c is determined by the point where the ray intersects the shock wave. The index of refraction, n, which is related to pressure by $\epsilon = 10^{-5}p$, can be made a function of the radius.

To adapt equation (5) to the specific case of the hydraulic ram shock phase it is necessary to carefully define the various geometric parameters involved. Figure 9 illustrates the angles and radii necessary to apply equation (5). Note that the diagram is symmetric about r* at angle ξ_1 .

A functional form for n(r) can be assumed. For example, a parabolic relation would be

$$n(r) = ar^2 + br + c$$

In order to evaluate the constants a, b, and c, the integral of equation (5) must be evaluated and iterated with geometric relations. This is quite complicated . In lieu of a parabolic relation a linear formula is used. This has the merit of a straightforward solution. One of the two parameters, i.e. A, can be determined leaving B to be found as the following manipulations show.

Assume (Fig. 9)

$$n = A + B\frac{r}{r'} \qquad r = r', \; n = n_2$$

$$n_2 = A + B$$

$$\therefore \quad n = n_2 + B\left(\frac{r}{r_1} - 1\right) \tag{6}$$

From the law of Bouguer

$$nr\sin\phi = \text{constant}$$

$$n_2 r \sin\phi_2' = n^* r^* \sin\phi^* = n^* r^*$$

$$n_2 r' \sin\phi_2' = \left[n_2 + B\left(\frac{r^*}{r_1} - 1\right) r^*\right] \tag{7}$$

From analytic geometry and Snell's law

$$\frac{\sin\beta_1}{\sin\beta_2} = \frac{n_2}{n_1} \tag{8}$$

$$\Delta\beta = \beta_1 - \beta_2 \tag{9}$$

$$\beta_1 = \frac{\pi}{2} - \theta' + \xi_1 + \Delta\beta \tag{10}$$

$$\beta_1 = \phi_2'' + \Delta\beta = \frac{\pi}{2} - \theta'' - \xi_1 - \Delta\beta + \alpha \tag{11}$$

$$\alpha = 2\xi_1 + 2\Delta\beta \tag{12}$$

$$\beta_1 = \frac{\pi}{2} - \theta'' - \xi_1 - \Delta\beta + 2\xi_1 + 2\Delta\beta$$

$$\therefore \beta_1 = \frac{\pi}{2} - \theta'' + \xi_1 + \Delta\beta \tag{13}$$

From Figure 9 with $\alpha, y_0, r', n_1, n_2$ known

$$y_0 + y_1 + y_2 = r' \sin\beta_1$$

$$y_0 + y_1 = r'' \sin(\beta_1 - \alpha) = r' \sin(\beta_1 - \alpha) \tag{14}$$

$$y_2 = r' \sin\beta - r' \sin(\beta - \alpha) = r'\left[\sin\beta' - \sin(\beta' - \alpha)\right] \tag{15}$$

$$\phi_2' + \beta_1 = \pi + \Delta\beta$$

$$\therefore \phi_2' = \pi + \Delta\beta - \beta_1 \tag{16}$$

$$\tan\alpha = \frac{y_1}{L_1 - \ell_1} \; ; \quad y_1 = \tan\alpha\left[L_1 - \ell_1\right]$$

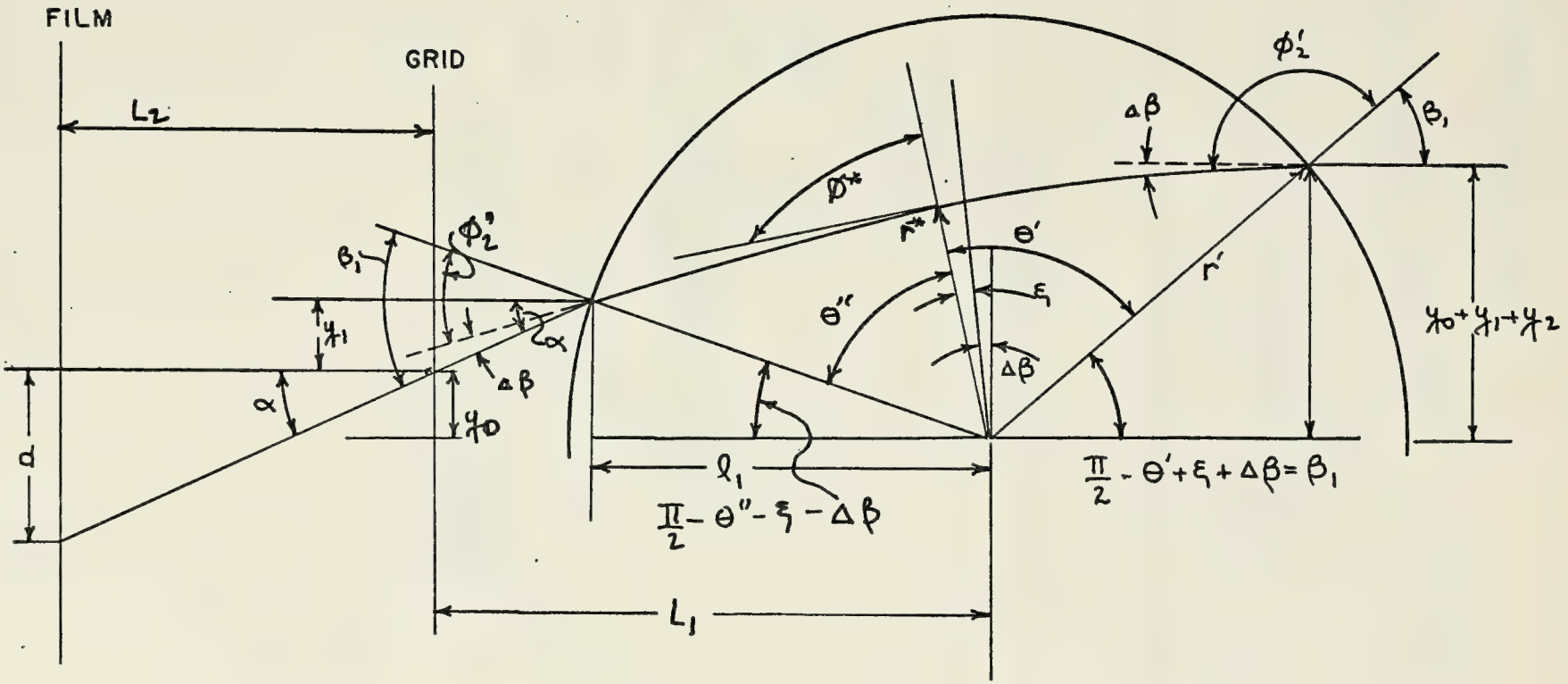

Fig. 9 Geometry of Light Ray

$$y_1 = \left[L_1 - r' \cos(\beta_1 - \alpha)\right] \tan\alpha$$

$$\therefore\ y_1 = \left[L_1 - r' \cos(\beta_1 - \alpha)\right] \tan\alpha$$

and

$$y_0 = r' \sin(\beta_1 - \alpha) - \left[L_1 - r' \cos(\beta_1 - \alpha)\right] \tan\alpha \qquad (17)$$

With the following substitutions, the solution for θ is

$$\theta = c \int \frac{dr}{\left[(A^2 + 2AB'r + B'r^2) r^2 - c^2\right]^{\frac{1}{2}}}$$

$$c = n_2 r' \sin\phi_2'$$

$$B' = \frac{B}{r'}$$

$$\theta = c \int_{r=r^*}^{r=r} \frac{dr}{r\left[B'r^4 + 2AB'r^3 + A^2r^2 - c^2\right]^{\frac{1}{2}}}$$

$$n_2 r' \sin\phi_2' = \left[n_2 + B\left(\frac{r^*}{r'} - 1\right)\right] r^* \qquad (18)$$

$$\theta' = c \int_{r=r^*}^{r=r} \frac{dr}{r\left[B^2 r^4 + 2AB'r^3 + A^2 r^2 - c^2\right]^{\frac{1}{2}}} \qquad (19)$$

Using a pressure behind the shock wave of 400 kg/cm^2, n_2 was found to be 1.335. See Figure 6 for data used in these calculations: r' is 7.62 cm. As shown in the Appendix the value for B is -0.04947. Using the equation for the linear pressure distribution it is calculated that p is 3646 kg/cm^2 at $\frac{r}{r'}$ 0.1267. The pressure increases toward the projectile nose. This result is consistent with Figure 29 of Holm's thesis (Ref. 2).

Results from fluid mechanics indicate that linear relations for p(r) and n(r) are not appropriate. Consequently the calculated pressure at $\frac{r}{r'}$ = 0.1267 is probably not correct. This analysis gives the correct trends. The difference between experimental and calculated values is considered to result from the assumed distribution for n.

C. WALL RESPONSE BY FIBER OPTICS PROXIMITY PROBES

The structural response of the entrance wall during the shock phase has been investigated and is presented in Refs. 4,5, and 6. Since the shock wave is a pressure disturbance propagating through the fluid medium, it is also by definition a stress wave. Types of stress waves include compression, tension and shear waves. The compression and tension waves involve positive and negative pressures, respectively, where the media particle motion is in the direction of wave propagation. The shear wave involves particle motion that is normal to the wave direction. Compression and tension waves are also known as dilatation waves while shear waves are sometimes called distortion waves. Tension waves that reduce compressed areas are also known as rarefaction waves (Ref. 3). Loads transmitted through the tank's

structural members are initially transmitted as stress waves of both dilatation and shear form. The outward motion of the entrance wall somewhat relieves the pressure disturbances (stress waves) acting on the wall. To measure the outward displacement of the wall a system based on optical glass fiber bundles was constructed. The optic fiber bundles were arranged coaxially with the transmitting bundle on the inside. This light was then directed onto the aluminum entrance wall. The reflected light was collected and transmitted by the output fiber bundle to an RCA 931A photomultiplier tube and a Pacific Photometric Model 11 laboratory photometer. The fiber bundles were three feet in length and were comprised of three-mil flint glass fibers with an index of refraction of 1.62 and a cladding glass of index 1.52. The corresponding numerical aperture was 0.56 with an acceptance cone half angle of approximately 34 degrees. The glass bundles were secured in a mounting bracket and placed over the entrance wall on a radial line emanating from the projectile impact point. The mounting bracket allowed for positioning the bundles up to a maximum of nine inches from the impact point. To increase the intensity of reflected light the entrance wall was hand polished with #500 Wetordry Tri-M-ite paper, then with Crystalbay Crocus cloth. The signal output of the photomultiplier was transmitted to a dual beam oscilloscope fitted with a Polaroid camera.

Initial calibration of the system was accomplished by mounting the fiber bundles in a platform micrometer. The light was reflected from a circular aluminum disk of the type used for the entrance wall. This disk was similarly polished. A calibration curve of volts versus the distance separating the disk and glass bundles was obtained, Figure 10.

Subsequent investigation of this system, modified to include a "chopper wheel", revealed an unacceptably low rise time for the photomultiplier tube. A Pacific Photometric Model 62 multiplier tube (RCA model 6199) was substituted; a Spectrum Physics model 132 HeNe laser replaced the light bulb. The inherent noise in the latter system obliterated the oscilloscope trace, rendering this optical fiber concept useless without further development to improve signal-to-noise ratio.

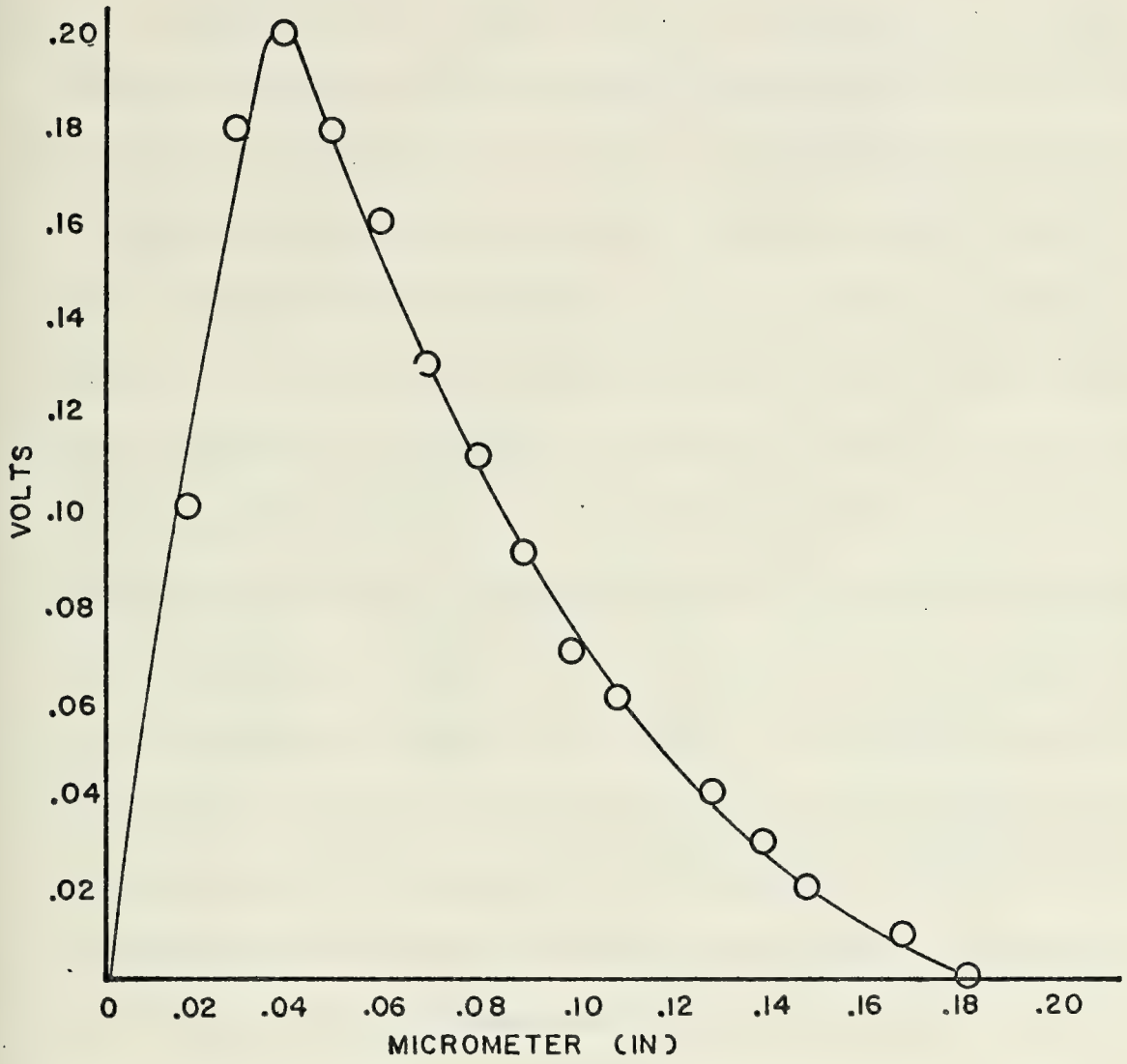

Fig. 10 Calibration Curve for Optical Fiber Proximity Probe

III. CORRELATION OF OSCILLATION PERIOD, CAVITY SIZE, AND ENERGY DISSIPATION DURING CAVITY PHASE

A. TECHNICAL APPROACH TO CORRELATION

In displacing water from its path, the projectile imparts a radial velocity to the water. The momentum associated with this velocity field is sufficiently high to cause the flow to separate from the projectile and to continue to expand causing a cavity. Fluid pressures caused by the tank boundaries eventually halt the cavity's expansion. At this point most of the kinetic energy initially associated with the velocity field has been converted to stored energy, gravitational potential energy and deformation of the tank's wall. These forces cause the cavity to start to collapse radially and, as the cavity shrinks, the fluid velocity increases resulting in the conversion of stored energy into kinetic energy and work in compressing gas trapped in the cavity. Since projectile impact was near the center of the tank the cavity would first neck down until a nearly spherical shape resulted. The sphere would then tend to collapse to a point until the pressures in the cavity halted this inward motion. Air which entered the cavity through the entrance wall hole is trapped and compressed to a high pressure at the instant of minimum cavity volume. A high pressure shock wave then propagates radially outward from the collapse point. After the pressure wave generated by the collapse subsides, the compressed air causes the cavity to re-expand. This cycle repeats several times until all the stored energy is dissipated (Refs. 6 and 7). Various authors, Lundstrom,

Stepka and Cardea, et al., have likened the cavity phase to underwater explosions. Using the method presented by Cardea and Cole, an analysis was made of a high speed film showing 0.30 cal and 14.5 mm rounds impacting a 6061T6 aluminum entrance wall. The film was obtained from Naval Weapons Center. These values were then compared with the analytical solutions obtained by Holm's research at NPS. Two significant variations were noted. Reference 7, equation (7), presents the maximum cavity radius as $a_M = .59T\left(\frac{P_0}{\rho_0}\right)^{1/2}$. A constant of .544 is considered to be more accurate. This difference accounts for an 8% variation in tabulated results shown as Table 2. Secondly, this paper considers the effects of projectile impact through a pre-punched aluminum entrance wall whereas the 0.30 cal and 14.5 mm rounds impacted a solid tank wall. For the latter the shock wave is generated by the impact of the projectile on the wall vice the fluid medium. The generation and propagation will be identical except for wall density and sonic velocity effects. This problem is addressed in Reference 3. The analysis of the 14.5 mm round must be considered as approximate as the maximum cavity radius to be measured extended beyond the frame size of 16 mm film.

B. DATA OBTAINED FROM MOVIE FILM

For each sequence of the 16 mm film obtained from the Naval Weapons Center, China Lake, the maximum cavity radius and time for one complete oscillation were measured. Using underwater explosion theory (Ref. 8) the energy required to expand the cavity was obtained first as a function

of cavity radius and second as a function of the cavity period. A theoretical value for the cavity radius was also calculated. These results were then compared with those obtained by Cardea (Ref. 7).

C. RESULTS

Table 2 lists the results obtained from the above measurements. The conclusion equating the cavity phase of hydraulic ram to underwater explosions appears valid.

For a comparison of the time required for one complete cavity oscillation, Reference 2 presents

$$t = \frac{2.62\, a_m}{\left[\frac{2}{3}\,\frac{P_\infty}{\rho}\right]^{\frac{1}{2}}}$$

where a_m is the measured cavity radius. From Reference 8 this time is given as

$$t = \frac{1.14\, \rho_0^{\frac{1}{2}} \left(\frac{4}{3}\pi\right)^{\frac{1}{3}} a_m}{P_0^{5/6}}$$

where

$P_0 =$ 2210 psf

$\rho_0 =$ 1.04 slugs

Evaluating the constants yields

$$t = 3.2\, a_m \left(\frac{\rho}{P_\infty}\right)^{\frac{1}{2}}$$

$$t = 1.84\, a_m \left(\frac{\rho_0}{P_0}\right)^{\frac{1}{2}}$$

respectively. It can be seen that the only difference in characteristic times is in the constants. Based on results of analysis of the film, equation is considered more correct.

0.30 cal Shot number	t millisec's	a_m measured Ft	a_m calc Ft	Ec=f(Am) Ft-lbs	Ec=f(T) Ft-lbs
1	24.8	.485	.455	874.78	874.81
2	22.0	.555	.404	610.68	610.70
3	28.1	.632	.516	1272.5	1272.6
4	28.8	.656	.529	1370.0	1370.1
5	29.1	.632	.534	1413.3	1413.3
14.5 mm Shot number					
1	46.9	1.125	.861	5916.5	5916.7
2	48.3	1.094	.887	6462.3	6462.5
3	47.4	1.007	.870	6107.7	6107.7
4	44.4	1.234	.815	5019.9	5020.1
5	45.5	1.266	.836	5402.3	5402.5
6	43.9	1.234	.806	4852.2	4852.4

Table 2 Cavity Period, Maximum Cavity Radius, Cavity Energy from Movie Film

0.50 cal Shot Number	t millisec's	a_m observed	a_m calc	Ec Ft-lbs
2	24.8	.5	.494	876.0
3	26.2	.5	.522	1032.0
4	26.9	.5	.536	1117.0
5	26.9	.5	.536	1117.0

Table 3 Cavity Period, Maximum Cavity Radius, Cavity Energy from Cardea (Ref. 7)

VI. CONCLUSIONS AND PROPOSED RESEARCH

A. CONCLUSIONS

Secondary shocks will occur in fuel cells penetrated by fragmentation warheads.

The mathematical model proposed for analyzing the optical grid distortion yields correct trends. Further development of an assumed distribution for the index of refraction is warranted.

Comparison of the cavity phase of hydraulic ram to underwater explosions provides valid relationships between cavity radius, energy and period of oscillation.

B. PROPOSED RESEARCH

HIGH SPEED FRAMING CAMERA

A high speed framing camera capable of 200,000 frames per second has been obtained. When incorporated into the existing test set-up, a complete time history of the shock front and projectile penetration will be available.

STRAIN GAGES

The existing entrance wall has been redesigned and fitted with several strain gages. Proposed research with this entrance wall should yield information on wall deflections and wall bending moments caused by projectile penetration.

APPENDIX A

SAMPLE CALCULATIONS FOR THE GRID DISTORTION ANALYSIS

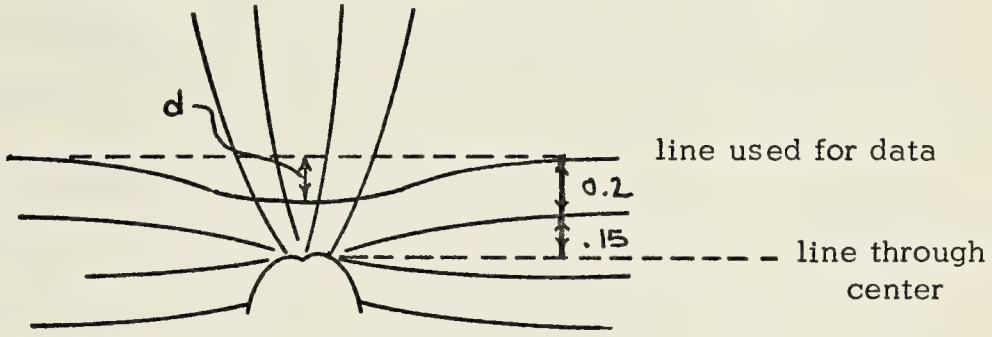

Fig. 12 Enlarged Grid Distortion

Steps for obtaining a solution:

1. evaluate equation (17) to find β_1
2. evaluate equations (8) and (9) to find β_2 and $\Delta\beta$
3. evaluate equation (12) to get ε_1
4. evaluate equations (10) and (13) for θ' and θ''
5. evaluate equation (14) to get ψ_1
6. evaluate equation (15) to get ψ_2
7. evaluate equation (16) for ϕ_2'
8. evaluate equation (11) for ϕ_2''
9. draw a curve of B vs r* using equation (18)
10. using number pairs (B,r*) from step 9, evaluate equation (19) for the right hand side. Iterate until correct (B,r*) are found.

From Figs. 11 and 12

d = 0.1 inch

L_2 = 19.8 inches

L_1 = 9 inches

y_0 = .35 inches

r' = 3 "

P = 400 kg/cm^2

$\therefore \alpha = \frac{(0.1)\ (180)}{(19.8)} = 0.29^\circ = .005$ radians

From equation (17)

$$0.35 = 3\sin(\beta_1 - \alpha) - [9 - 3\cos(\beta_1 - \alpha)]\tan\alpha$$

Assume $(\beta_1 - \alpha)$ is small

$$\therefore \quad 0.35 \cong 3(\beta_1 - \alpha) - (9-3)\alpha$$

$$3\beta_1 = .35 + 9\alpha$$

or $\beta_1 = \frac{0.35}{3} + 3\alpha = .1318$ radians

try $\beta_1 = 7.55^\circ$

$\beta_1 - \alpha = 7.55^\circ - 0.29 = 7.26^\circ$

then

$$0.35 \stackrel{?}{=} 3\sin 7.26 - [9 - 3\cos 7.26](\tan 0.29) = .3486$$

from iteration

$\beta_1 = 7.57^\circ$

$$\therefore \sin\beta_2 = \sin\beta_1 \left(\frac{n_2}{n_1}\right)^{-1} = \sin\beta_1 \left(\frac{n_1}{n_2}\right)$$

Using p = 400 kg/cm^2 at r' = 3 inches

$\epsilon = 10^{-5} p = 0.004$

$n_2 = n_1(1 + .004) = 1.33\,(1.004)$

$n_2 = 1.3353$

$\therefore \frac{n_1}{n_2} = \frac{1.33}{1.3353} = 0.9960$

then

$\sin\beta_2 = [\sin(7.57°)](.9960)$

$\sin\beta_2 = .13121$

$\therefore \beta_2 = 7.5183°$

$\Delta\beta = \beta_2 - \beta_1 = 7.57° - 7.5183°$

$\Delta\beta = 0.0517°$

from equation (12)

$\xi_1 = \frac{\alpha}{2} - \Delta\beta$

$\xi_1 = \frac{.29}{2} - .0517 = 0.0933°$

from equation (10)

$\theta' = 90 + \xi_1 + \Delta\beta - \beta_1 = 90 + .0933 + .0517 - 7.57$

$\theta' = 82.575°$

from equation (13)

$\theta'' = 90 + \xi_1 + \Delta\beta - \beta_1 = 82.575°$

from equation (14)

$y_1 = r'\sin(\beta_1 - \alpha) - y_0 = 3\sin(7.57 - .29) - .035$

$y_1 = 0.03''$

from equation (15)

$$y_2 = 3[\sin 7.57 - \sin(7.57 - .29)]$$

$$y_2 = 0.015''$$

from equation (16)

$$\phi_2' = 180 + .05 - 7.57$$

$$\phi_2' = 172.4817^\circ$$

from equation (11)

$$\phi_2'' = \beta_1 - \Delta\beta = 7.57 - .0517$$

$$\phi_2'' = 7.5183^\circ$$

An approximation for B is

$$r^* = y_0 + y_1$$

$$\therefore \frac{r^*}{r'} = \frac{y_0 + y_1}{r'} = \frac{0.35 + 0.03}{3} = .1267$$

from step (9)

$$B = -n_2 \left[\frac{\sin\phi_2' - \frac{r^*}{r'}}{\left(\frac{r^*}{r'} - 1\right)\frac{r^*}{r'}} \right]$$

$$B = \frac{(-1.3353)(.1308 - .1267)}{(.1267)(1 - .1267)}$$

$$B = -0.04947^\circ$$

from the assumed distribution for n

$$n = n_2 + B\left(1 - \frac{r}{r'}\right)$$

$$n = 1.3353 + 0.04947\,(1 - .1267) \quad \text{when} \quad r = r^*$$

$$\therefore n = 1.3785$$

then

$$\epsilon = \frac{\Delta n}{n} = \frac{n_1 - n_1}{n_1}$$

$$\epsilon = \frac{1.3785 - 1.33}{1.33}$$

$$\epsilon = 0.03646$$

but

$$\epsilon = 10^{-5} \Delta p$$

$$\therefore p = 10^5 (0.03646)$$

$p = 3646.78$ kg/cm^2 (calculated for a radius ratio of $\frac{r}{r_1} = 0.1267$)

```
C
C     RR-  NONDIMENSIONAL RADIUS
C     XN1- REFRACTION INDEX OF WATER, CONSTANT=1.33
C     XN2- REFRACTIVE INDEX BASED ON SNELL'S LAW
C     PRE- PRESSURES EXTRACTED FROM PREVIOUS THESIS
C     THETA1- ENTRY ANGLE, RADIANS
C     THETA2- EXIT ANGLE, RADIANS
C     ANS1- ENTRY ANGLE, DEGREES
C     ANS2- EXIT ANGLE, DEGREES
C     RES- THETA1-THETA2 TIMES 2
C
      DIMENSION PRE(9),RR(9),THETA1(9),THETA2(9),B(9),E(9),XN2(9)
      DIMENSION XX(9),ANS1(9),ANS2(9),RES(9)
      XN1=1.33
      DO 10 J=1,9
      READ (5,502) PRE(J)
      WRITE (6,502) PRE(J)
      WRITE (6,501)
      SUM=0.0
      E(J)=1.0E-5*PRE(J)
      XN2(J)=XN1*(1.0 + E(J))
      B(J)=1.0/(1.0 + E(J))
      DO 20 I=1,9
      SUM=SUM + .1
      RR(I)=SUM
      THETA1(I)=ARSIN(RR(I))
      ANS1(I)=THETA1(I)*57.3
      XX(I)=B(J)*RR(I)
      THETA2(I)=ARSIN(XX(I))
      ANS2(I)=THETA2(I)*57.3
      RES(I)=(ANS1(I)-ANS2(I))*2.
      WRITE (6,503) RR(I),THETA1(I),THETA2(I),ANS1(I),ANS2(I),RES(I)
   20 CONTINUE
   10 CONTINUE
      WRITE (6,504) XN2
  501 FORMAT('0',4X,'RR',8X,'THETA1',4X,'THETA2',4X,'ANS1',5X,'ANS2',7X
     1,'RES')
  502 FORMAT(F8.2)
  503 FORMAT(6F10.3)
  504 FORMAT('0',4X,'XN2= ',F7.4)
      STOP
      END
```

BIBLIOGRAPHY

1. McMillen, J. H., "Shock Wave Pressures in Water Produced by Impact of Small Spheres", Physical Review, v. 68, numbers 9 and 10, p. 198-203, 1 and 15 November 1945.

2. Holm, D.P., Hydraulic Ram Shock Waves and Cavitation Effects on Aircraft Fuel Cell Survivability, M.S. Thesis, Naval Postgraduate School, Monterey, 1973.

3. Boeing Technical Proposal D180-15046-1, Investigation of Ballistic Damage Tolerant Fuel Tanks by Research and Engineering Group, Aerospace Division, The Boeing Company, 15 June 1972.

4. Ball, R.E., "A Program for the Nonlinear Static and Dynamic Analysis of Arbitrarily Loaded Shells of Revolution," Computers and Structures, v. 2, 1972.

5. McDonnell Aircraft Corporation Report G964, Hydraulic Ram: A Fuel Tank Vulnerability Study by R. Yurkovitch, 5 Sept 1969.

6. Naval Weapons Center Technical Publication 5227, Fluid Dynamic Analysis of Hydraulic Ram, E.A. Lundstrom, July 1971.

7. Cardea, G.C., The Cavitation Phase of Hydraulic Ram Described by Equations Derived for Underwater Explosions, M.S. Thesis, Air Force Institute of Technology, Wright-Patterson Air Force Base, Ohio, 1973.

8. Cole, R.H., Underwater Explosions, Princeton University Press, 1945.

9. Stanford Research Institute Project PGD 7708, Shock Effects in Fuel Cells by Roger P. Williams, October 1969.

10. Naval Weapons Center film 3045, dated 23 March 1973.

11. The Boeing Company Report D162-10294-1, Hydraulic Ram, by R.G. Blaisdell, 18 Sept 1970.

INITIAL DISTRIBUTION LIST

		No. Copies
1.	Defense Documentation Center Cameron Station Alexandria, Virginia 22314	2
2.	Library (Code 0212) Naval Postgraduate School Monterey, California 93940	2
3.	Chairman, Department of Aeronautics (Code 57) Naval Postgraduate School Monterey, California 93940	1
4.	Professor A. E. Fuhs, Code 57Fu Department of Aeronautics Naval Postgraduate School Monterey, California 93940	5
5.	Captain Larry S. Mueller 5N206 Ridgewood Bensenville, Illinois 60106	2
6.	Dr. Eric Lundstrom Code 3104 Naval Weapons Center China Lake, California 93555	4
7.	Professor H. Power, Code 57Ph Department of Aeronautics Naval Postgraduate School Monterey, California 93940	2
8.	Professor R. Ball, Code 57Bp Department of Aeronautics Naval Postgraduate School Monterey, California 93940	2
9.	Captain James McNerney DDR & E Pentagon Department of Defense Washington, D. C. 20301	1

10.	Colonel James Thompson USAF WSEG/IDA 400 Army Navy Drive Arlington, Virginia 22202	1
11.	CDR Merlin L. Johnson Naval Air Systems Command Washington, D.C. 20360	1
12.	CDR D. Hicks Naval Air Systems Command Washington, D. C. 20360	1
13.	Robert G. Clodfelter AFAPL Wright-Patterson AFB, Ohio 45433	1
14.	Robert G. Blaisdell Structures R&D Program Manager Boeing Aerospace Group P.O. Box 3999 Seattle, Eashington 98124	1

REPORT DOCUMENTATION PAGE		READ INSTRUCTIONS BEFORE COMPLETING FORM
1. REPORT NUMBER	2. GOVT ACCESSION NO.	3. RECIPIENT'S CATALOG NUMBER
4. TITLE (and Subtitle) Experimental Investigation of Hydraulic Ram		5. TYPE OF REPORT & PERIOD COVERED Masters Thesis March 1974
		6. PERFORMING ORG. REPORT NUMBER
7. AUTHOR(s) Larry Scott Mueller		8. CONTRACT OR GRANT NUMBER(s)
9. PERFORMING ORGANIZATION NAME AND ADDRESS Naval Postgraduate School Monterey, California 93940		10. PROGRAM ELEMENT, PROJECT, TASK AREA & WORK UNIT NUMBERS
11. CONTROLLING OFFICE NAME AND ADDRESS Naval Postgraduate School Monterey, California 93940		12. REPORT DATE March 1974 13. NUMBER OF PAGES 47
14. MONITORING AGENCY NAME & ADDRESS(if different from Controlling Office)		15. SECURITY CLASS. (of this report) Unclassified 15a. DECLASSIFICATION/DOWNGRADING SCHEDULE

16. DISTRIBUTION STATEMENT (of this Report)

Approved for public release; distribution unlimited.

17. DISTRIBUTION STATEMENT (of the abstract entered in Block 20, if different from Report)

Unclassified-unlimited

18. SUPPLEMENTARY NOTES

19. KEY WORDS (Continue on reverse side if necessary and identify by block number)

Hydraulic ram, aircraft survivability,shock waves, projectile damage

20. ABSTRACT (Continue on reverse side if necessary and identify by block number)

Extensions of the investigations aimed at preventing aircraft destruction through the effects of hydraulic ram were conducted. By analyzing spark shadowgraphs the existence of a family of transient shock waves was confirmed. These shock waves were created by a surface anomaly in a projectile and are not unlike those found in fragmentary warheads. In an attempt to measure wall deflections subsequent to projectile impact,

a system based on optical fiber proximity probes was investigated. Mathematical models based on grid distortions were used as a means of calculating shock wave pressures. The AFIT thesis correlating cavity size, energy and radius to underwater explosions was verified from an analysis of 16 mm films.

Thesis
M8837
c.1

151162

Mueller
Expermental investigation of hydraulic ram.